Effects of Amorphous Poly(3-hexylthiophene) on Active-Layer Structure and Solar Cells Performance

Chung-Hao Liu,[1] Wei-Hsuan Tseng,[2] Chih-Yang Cheng,[1] Chih-I Wu,[2]
Pi-Tai Chou,[3] Shih-Huang Tung[1]
[1]Institute of Polymer Science and Engineering, National Taiwan University, Taipei, Taiwan 10617
[2]Institute of Photonics and Optoelectronics and Department of Electrical Engineering, National Taiwan University, Taipei, Taiwan 10617
[3]Department of Chemistry and Center of Emerging Material and Advanced Devices, National Taiwan University, Taipei, Taiwan 10617
Correspondence to: S.-H. Tung (E-mail: shtung@ntu.edu.tw)

Received 29 September 2015; accepted 22 December 2015; published online 30 January 2016
DOI: 10.1002/polb.23999

ABSTRACT: A key challenge to the development of polymer-based organic solar cells is the issue of long-term stability, which is mainly caused by the unstable time-dependent morphology of active layers. In this study, poly(3-hexylthiophene) (P3HT)/[6,6]-phenyl C60-butyric acid methyl ester (PCBM) blend is used as a model system to demonstrate that the long-term stability of power conversion efficiency can be significantly improved by the addition of a small amount of amorphous regiorandom P3HT into semicrystalline regioregular one. The optical properties measured by UV–vis absorption and photoluminescence reveal that regiorandom P3HT can intimately mix with PCBM and prevent the segregation of PCBM. In addition, X-ray scattering techniques were adopted to evidence the retardation of phase separation between P3HT and PCBM when regiorandom P3HT is added, which is further confirmed by optical microscopy that shows a reduction of large PCBM crystals after annealing at high temperature in the presence of regiorandom P3HT. The improvement of the long-term stability is attributed to the capability of amorphous P3HT to be thermodynamically miscible with PCBM, which allows the active layer to form a more stable structure that evolves slower and hence decelerates the device decay. © 2016 Wiley Periodicals, Inc. J. Polym. Sci., Part B: Polym. Phys. **2016**, *54*, 975–985

KEYWORDS: amorphous; amorphous P3HT; blends; conjugated polymers; miscibility; morphology; SAXS; solar cell; stability

INTRODUCTION Recent advance in organic solar cells has greatly benefited from the development of bulk heterojunction architecture for polymer/fullerene blends.[1] The widely accepted inference for the success of bulk heterojunction organic solar cells is that such an architecture happens to form bicontinuous well-packed polymer and fullerene domains on a scale of ~10 nm, which facilitate charge carrier separation at the facilely accessible interfaces as well as the transport of holes and electrons to electrodes through the fine continuous pathways.[2–5] In addition, it has been shown that a molecularly intermixed amorphous phase of polymer and fullerene is crucial to the performance of organic solar cells because a much faster charge separation process predominantly occurs in these regions.[6–9] Although some nearly amorphous conjugated polymers have been reported to work well in bulk heterojunction organic solar cells,[10,11] most of the high-performance devices are fabricated by semicrystalline polymers which contains both crystalline and amorphous domains to allow the optimal structure to be achieved when blended with an appropriate amount of fullerene.

The power conversion efficiency (PCE) of polymer/fullerene composite organic solar cells has recently exceeded 10% for single-layer devices fabricated under solution processing.[12–15] The increase of the device lifespan, however, remains a key challenge. Each component of the devices may raise the instability issues, among which the degradation of active layers is considered to be the major cause. The degradation of the active layers originates partly from the photolytic and photochemical reactions of the organic materials, especially in the presence of oxygen and water from atmosphere.[16] The other main problem responsible for the short lifetime is that the optimal structures in active layer, that is, the coexistence of fine crystalline polymer and fullerene channels as well as molecularly intermixed regions, are not

Additional Supporting Information may be found in the online version of this article.

in a thermodynamically stable state, but a nonequilibrium state kinetically frozen during device processing. In other words, the morphology inevitably changes with time toward an equilibrium, especially at high temperature.[17–19] The morphological transition has been suggested to involve a large-scale aggregation of fullerene that reduces the interfacial area for charge generation, and thus leads to a decay of PCE.[20]

Taking the most widely studied regioregular poly(3-hexylthiophene)/[6,6]-phenyl C60-butyric acid methyl ester (P3HT/PCBM) blending system as an example, the macrophase separation between polymer and fullerene results from a combination of two aspects. First, regioregular P3HT is a semicrystalline polymer and upon crystallization, the impurities, such as PCBM, are expelled by the growing P3HT crystals.[21] This is valid for most polymer/fullerene blends, except for the polymers with large space between the side chains where fullerenes can intercalate to form cocrystals.[22,23] The rejected PCBM accumulates in amorphous P3HT and the PCBM concentration there is thus increased. Second, although amorphous P3HT and PCBM are miscible, the amount of PCBM existing in the interlamellar amorphous P3HT regions is limited due the restrain of P3HT tie chains.[24,25] There is a threshold concentration for PCBM to dissolve in the interlamellar amorphous P3HT regions, above which a phase separation occurs and the aggregates may be in a scale larger than the exciton diffusion length so that efficiency decreases accordingly.[2]

Many efforts have been made to retard the phase separation in polymer/fullerene blends so as to enhance the stability of devices, including the crosslinking of polymer to fix the structure,[26,27] the chemical modification of fullerene to lower the diffusion rate,[28–30] and the incorporation of additives or functional groups to enhance the miscibility between polymer and fullerene.[31,32] In addition, an increase of the amorphous fraction of polymer has been shown to be a strategy to efficiently improve the stability.[33] This was carried out by the synthesis of a series of P3HT with varying regioregularity to tune the crystallization ability, and the results show that the highly regioregular, crystalline P3HT leads to a severer phase segregation between P3HT and PCBM with increasing time than the lower regioregular P3HT does.[34] It is suggested that the introduction of disorder into the polymer backbone that reduces crystallinity can suppress the crystallization-driven phase separation and thus the devices display a better long-term thermal stability. The detailed nanoscale morphological transition, however, has not been fully characterized and requires to be further clarified.

Instead of the chemical synthesis route to create amorphous P3HT phase, we adopted a simple physical strategy, that is, the blending of highly regioregular P3HT (*rr*-P3HT) and amorphous regiorandom P3HT (*rra*-P3HT), to tune the fraction of crystalline and amorphous phases. Previous reports have shown that the addition of a significant amount of *rra*-P3HT into *rr*-P3HT/PCBM blends prevents the large PCBM aggregates.[24,25,35] However, the performance of such solar cells, especially the long-term stability, has not been systematically studied. In this work, we carefully examined the effect of *rra*-P3HT on the morphology, absorption, photoluminescence (PL), and solar cell performance of P3HT/PCBM blends. We find that with the addition of too much *rra*-P3HT, approximately above 10 wt % of total P3HT, the efficiency is considerably decreased. However, in the presence of a small amount of *rra*-P3HT, ∼5 wt %, the stability of the solar cells is enhanced while the initial PCE is almost the same as that of pure *rr*-P3HT/PCBM devices. We used the X-ray scattering techniques to probe the size of P3HT crystallites and gain an insight into their aggregation behaviors varying with time and temperature. The results and corresponding discussion provide a clear picture of the relationship between the performance of solar cells and the structure in active layers.

EXPERIMENTAL

Materials

Regiorandom P3HT (*rra*-P3HT) was purchased from Sigma-Aldrich and the number-average molecular weight determined by gel permeation chromatography (GPC) is ∼27 kg/mol. Regioregular P3HT (*rr*-P3HT) was purchased from Rieke Metals. The weight-average molecular weight, polydispersity index, and regioregularity are 21 kg/mol, 1.6, and >95%, respectively. [6,6]-Phenyl C60-butyric acid methyl ester (PCBM) and 1,2-dichlorobenzene (DCB) were purchased from Alfa Asear. All chemicals were used as received.

Sample Preparation

rr-P3HT, *rra*-P3HT, and PCBM in desired ratio were dissolved in DCB. These solutions were heated to 90 °C overnight to ensure complete dissolution. Thin films were spun-cast from the solutions at 900 rpm on silicon wafer for 40 seconds and the still wet films were slowly dried in the oven at 25 °C for 1 day. Thermal annealing was conducted at 140 °C for 10 min on hotplate. Bulk samples were prepared from the solutions dried at room temperature in Teflon beaker and then annealed at 140 °C. The sample name for *rr*-P3HT/*rra*-P3HT mixtures without PCBM are abbreviated as P-X while that for *rr*-P3HT/*rra*-P3HT/PCBM ternary blends with the weight ratio of total P3HT:PCBM = 1:1 are abbreviated as B-X, where X is the weight percentage of *rr*-P3HT in total P3HT. For example, the *rr*-P3HT:*rra*-P3HT:PCBM weight ratio for P-95 and B-95 sample are 0.95:0.05:0 and 0.95:0.05:1, respectively.

Photovoltaic Devices Fabrication

The solar cell devices were fabricated with inverted structure. For the preparation of aluminum-doped zinc oxide (AZO) thin film, 0.49 g zinc acetate dehydrate was mixed with 10 mg aluminum nitrate in 4-ml 2-propanol with ethanolamine as stabilizing agent. The solution was spun-cast on indium tin oxide (ITO)/glass substrate with a thickness ∼50 nm and then baked at 280 °C for 10 min in the oven to convert the zinc acetate and aluminum nitrate into AZO thin film. The active layers with a thickness ∼200 nm were then spun-cast from the solutions of different *rr*-P3HT:*rra*-P3HT ratio along with equal weight of PCBM. After thermal annealing at 140 °C for 10 min, a 1.5-nm hole transport molybdenum trioxide (MoO_3) layer and Ag electrode about 85 nm in thickness were deposited via thermal evaporation. The finished devices were placed in glove box and covered by aluminum foil to prevent the oxygen and light. The current density versus voltage (*J*–*V*) curves were measured under nitrogen atmosphere using a Keithley 2400 source measurement unit. The photocurrent was measured under AM 1.5 G 100 mW/cm^2 illumination from an ABET SUN2000 550 W solar simulator.

Optical Properties

Absorption spectra of solutions and thin films were characterized by a UV–vis spectrometer (UV-650, Jasco) and the range of wavelength is from 300 to 800 nm. The PL spectra were obtained using a spectrofluorimeter (Fluorolog, Jobin Yvon Horiba) excited at 500 nm in air. The wavelength of PL spectra ranges from 550 to 850 nm. For UV–vis and PL measurements, thin films were spun-cast on cleaned quartz substrates.

Imaging

Atomic force microscopy (AFM) imaging was conducted on a MultiMode AFM system with a Nanoscope 3D controller (Digital Instruments/Veeco Metrology) in the tapping mode. The spring constant of the cantilevers (Nanosensor PPP-NCHR) was $\sim$42 N/m and the resonant frequency was $\sim$330 kHz. Optical microcopy imaging was performed on an Olympus BX53 microscope. Samples were spun-cast on cleaned quartz substrates.

X-Ray Scattering

Grazing-incidence small-angle and wide-angle X-ray scattering (GISAXS and GIWAXS) for thin films were carried out on beamline B23A1 in the National Synchrotron Radiation Research Center (NSRRC), Taiwan. The wavelength λ was 0.86 Å and the incident angle was 0.15°. Tw-dimensional (2D) patterns were collected on Pilatus 1M-F and Hamamatsu C9728DK-10 for GISAXS and GIWAXS, respectively.[36] The scattering angle was calibrated using silver behenate as the standard. Line-averaged intensities are reported as the plots of scattering intensity I versus the scattering vector q, where $q = (4\pi/\lambda)\sin(\theta/2)$ and θ is the scattering angle. Transmission-mode small-angle and wide-angle X-ray scattering (SAXS and WAXS) for bulk samples were conducted on the same beamline. The 1D scattering intensity profiles were obtained by circularly averaging the 2D patterns.

RESULTS AND DISCUSSION

Absorption and Photoluminescence

We first discuss the UV–vis absorption of the samples in solutions and thin films. Figure 1(a) shows the spectra of the mixtures with different compositions of *rr*-P3HT and *rra*-P3HT in solutions where P3HT can be well dissolved so that the spectra reflect the absorption from isolated chains. Pure *rra*-P3HT (P-0) shows the absorption at 439 nm. When the content of *rr*-P3HT increases, the maximum absorption redshifts and reaches 463 nm for pure *rr*-P3HT (P-100). The absorption curves of P-95 and P-100 nearly overlap. It has been known that the *rr*-P3HT chains with regular head-to-tail configuration tends to adopt a more ordered, coplanar conformation while *rra*-P3HT chains undergo severe torsion due to the steric repulsion between side alkyl chains. This explains why *rr*-P3HT has a longer conjugation length and a lower energy absorption.[37]

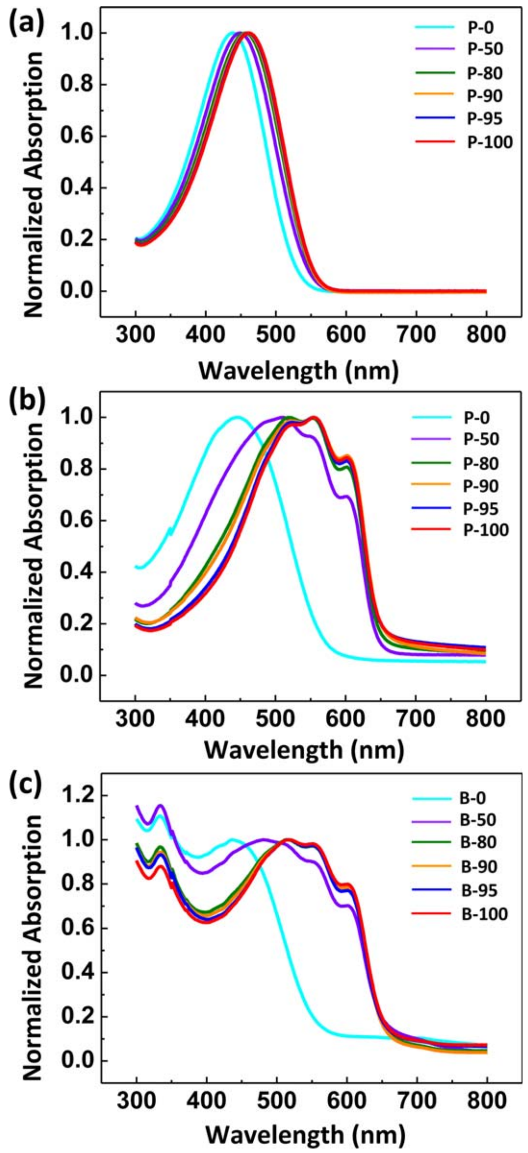

FIGURE 1 UV–vis absorption of (a) *rr*-P3HT/*rra*-P3HT mixtures in solution, (b) *rr*-P3HT/*rra*-P3HT thin films annealed at 140 °C for 10 min, and (c) *rr*-P3HT/*rra*-P3HT/PCBM ternary blends with equal weight of PCBM and total P3HT annealed at 140 °C for 10 min. [Color figure can be viewed in the online issue, which is available at wileyonlinelibrary.com.]

The spectra of thin films cast from solutions and annealed at 140 °C for 10 min are shown in Figure 1(b). The maximum absorption of P-0 thin film does not significantly change in comparison with that in solution (slight shift from 439 to 444 nm) because *rra*-P3HT is an amorphous polymer and the conformation of P3HT chains in amorphous state is similar to that of isolated chains in solutions. *rr*-P3HT is capable of forming crystals in thin films due to the highly regular chains. The crystalline parts yield two absorption maxima at longer wavelength region, 555 and 604 nm, respectively.[38] In P3HT crystallites, the extended chains prefer a planar conformation to minimize the conformational energy as well as to facilitate a close packing that minimizes the intermolecular interaction energy. The high degree of intrachain order increases the conjugation length and causes the maximum absorption of P-100 thin film at 555 nm whereas the interchain π-π stacking of *rr*-P3HT in crystallites results in the distinct absorption band at 604 nm.[39] In addition to the absorption of crystals, a band at lower wavelength (523 nm) is observed for P-100 thin film, which is attributed to the intrachain absorption of the less ordered chains in the amorphous region restrained by P3HT crystallites.[38] In the cases of P-50, P-80, and P-95 thin films, the same absorption bands at 555 and 604 nm found in P-100 sample can be seen and the intensity increases with *rr*-P3HT fraction due to the increase of crystallinity, implying that these two bands originate from *rr*-P3HT crystals. In contrast, the position of the amorphous band is composition-dependent and red-shifts with increasing *rr*-P3HT, suggesting that the amorphous phase is a mixture of *rra*-P3HT and uncrystallized *rr*-P3HT. Because of the shrinkage of the amorphous region with increasing *rr*-P3HT, a relative decrease in the absorption intensity of the amorphous bands can be observed. The change in the absorption spectra of *rr*-P3HT/*rra*-P3HT mixtures with varying compositions is analogous to those of P3HT intentionally synthesized with varying regioregularity.[33]

The thin film absorption spectra of *rr*-P3HT/*rra*-P3HT/PCBM ternary blends with equal weight of PCBM and total P3HT are shown in Figure 1(c). The peak around 335 nm is the absorption of PCBM aggregates. The presence of PCBM does not significantly affect the absorption bands of P3HT crystalline phase, still at 555 and 604 nm, because PCBM are excluded from P3HT crystals. The amorphous bands, however, are ~5-nm blue-shifted from that of *rr*-P3HT/*rra*-P3HT mixtures upon addition of PCBM. This observation implies that PCBM mixes in amorphous P3HT, which in turn reduces the intra or interchain order of P3HT and causes the blue-shift.[33] Comparing the spectra of B-80, B-90, B-95, and B-100 that are normalized to ~516-nm band, the absorption intensity of PCBM around 335 nm slightly reduces with increasing fraction of *rr*-P3HT. The weaker absorption has previously been attributed to the formation of larger PCBM crystals.[6,40] In other words, PCBM tends to aggregate in the presence of *rr*-P3HT. The rejection of PCBM from P3HT crystals may cause an excess of PCBM in amorphous P3HT matrix and thus lead to the crystallization of PCBM.[41]

Figure 2 shows the PL emission of the ternary blends excited at 500 nm. The emission between 600 and 800 nm drastically weakens when the fraction of *rra*-P3HT is increased, indicative of a more pronounced PL quenching for *rra*-P3HT. A high PL quenching infers a short distance that P3HT excitons require to diffuse before reaching PCBM for dissociation.[42] Therefore, an almost fully quenched PL for B-0 sample suggests that *rra*-P3HT intimately mix with PCBM in a molecular level, while in the pure *rr*-P3HT crystalline domains, the excitons have to diffuse a fairly long distance to reach PCBM boundaries so that a higher PL emission (lower PL quenching) is observed. As we will discuss later, the miscibility of *rra*-P3HT and PCBM is crucial to the stability of solar cell performance.

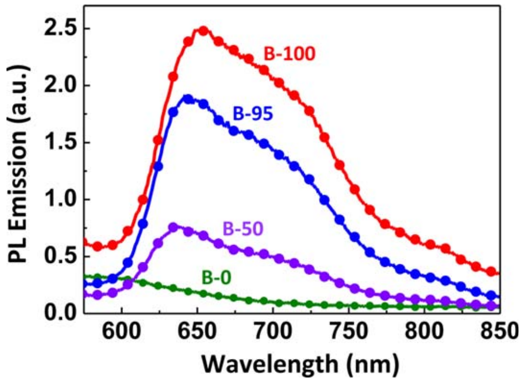

FIGURE 2 Photoluminescence spectra (PL) of *rr*-P3HT/*rra*-P3HT/PCBM ternary blends with equal weight of PCBM and total P3HT annealed at 140 °C for 10 min. [Color figure can be viewed in the online issue, which is available at wileyonlinelibrary.com.]

Thin-Film Structures

The grazing incidence wide-angle X-ray scattering (GIWAXS) is used to determine the structure and the orientation in thin films. Figure 3(a–d) shows the 2D GIWAXS patterns of *rr*-P3HT/*rra*-P3HT mixtures with varying compositions after thermal annealing. There is no diffraction spot for P-0 sample, indicating that *rra*-P3HT is amorphous and the chains lack ordering. For P-50, P-95, and P-100 samples, the (100), (200), and (300) diffraction spots of lamellar stacking can be clearly seen along q_z axis and the (010) of π-π stacking appears in q_y direction. *rr*-P3HT crystallizes in all the films and dominantly arranges in an edge-on manner with alky side chains perpendicular while the π-π stacking parallel to the substrate. Note that the diffraction peaks are sharper and stronger than those of as-cast films as compared in Supporting Information Figure S1, implying a thickening of P3HT crystallites and a more order stacking after thermal annealing. Figure 3(e–h) shows the GIWAXS patterns of the ternary blends after thermal annealing. The diffraction patterns look similar to those without PCBM, except that for all the films, the diffraction rings of PCBM clusters are observed at $q \sim 1.4$ Å^{-1}. The self-aggregation of PCBM into appropriate scale that facilitates the electron transport is required for organic bulk heterojunction solar cells to effectively function.[22,42] The unchanged d-spacing of P3HT crystallites in the presence of PCBM confirms that PCBM molecules are excluded from P3HT crystallites. The d-spacings of P3HT

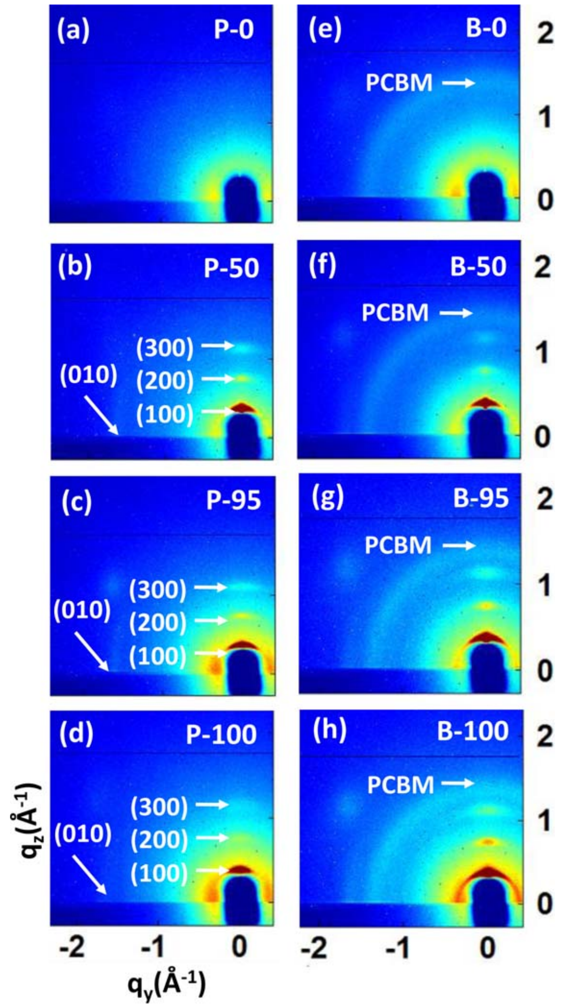

FIGURE 3 GIWAXS patterns of (a–d) *rr*-P3HT/*rra*-P3HT mixtures and (e–h) *rr*-P3HT/*rra*-P3HT/PCBM ternary blends with equal weight of PCBM and total P3HT. All films were annealed at 140 °C for 10 min. [Color figure can be viewed in the online issue, which is available at wileyonlinelibrary.com.]

crystallites in all the films are listed in Supporting Information Table S1.

The surface morphologies of the films were characterized by atomic force microscopy (AFM) and the height images of the samples after thermal annealing at 140 °C for 10 min are shown in Figure 4. The surface of P-0 is smooth, with a small root-mean-square (RMS) roughness ~0.42 nm, due to the amorphous nature of *rra*-P3HT that is unable to form the fibrous crystalline structure generally found in *rr*-P3HT. In P-50, P-95, and P-100 samples, the RMS roughness is apparently larger (>9 nm) and the roughness caused by the crystallites increases with increasing fraction of *rr*-P3HT. The height images of the ternary blends after thermal annealing are compared in Figure 4(e–h). The addition of PCBM has no significant effect on B-0 sample and the surface is still smooth, due to the low-surface tension P3HT that prefers to expose to air[43] as well as the miscibility of *rra*-P3HT and PCBM that prevents PCBM from large-scaled aggregation.[24] The RMS surface roughness is larger for B-50, B-95, and B-100 samples, similar to the trend without PCBM.

Solar Cell Performance and Stability

We fabricated the devices using the ternary blends as active layers in an inverted structure as described in the experimental section. Due to the lack of ordered packing and the low electron mobility for *rra*-P3HT, the power conversion efficiencies of the ternary blends with *rr*-P3HT fraction below 75% of total P3HT are rather poor (data not shown). We thus only discuss the photovoltaic performance of the devices with *rr*-P3HT above 80%. Figure 5 shows the *J–V* characteristics of the devices made from the blends after thermal annealing at 140 °C for 10 min. The PCEs are 1.39, 0.99, 3.21, and 3.26% for B-80, B-90, B-95, and B-100, respectively. Neat *rr*-P3HT with PCBM shows the highest

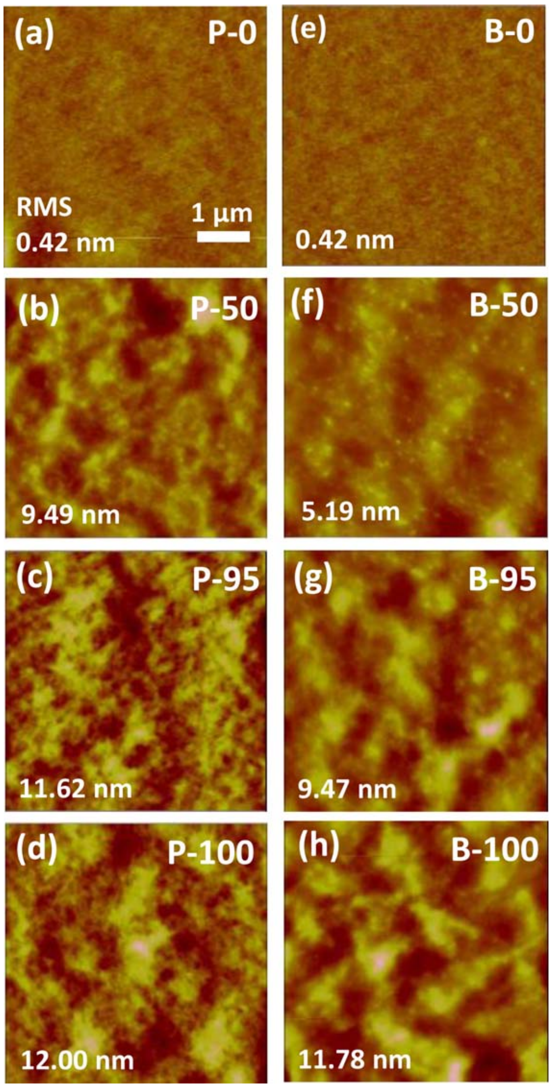

FIGURE 4 AFM height images of (a–d) *rr*-P3HT/*rra*-P3HT thin films and (e–h) *rr*-P3HT/*rra*-P3HT/PCBM ternary blends with equal weight of PCBM and total P3HT. All films were annealed at 140 °C for 10 min. [Color figure can be viewed in the online issue, which is available at wileyonlinelibrary.com.]

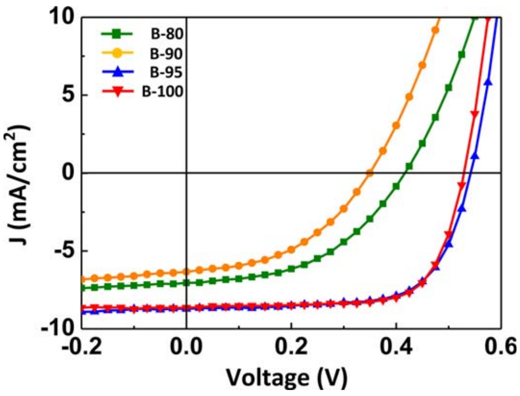

FIGURE 5 J–*V* characteristics of the optimized devices made from B-80, B-90, B-95, and B-100 samples after annealing at 140 °C for 10 min. The V_{oc}, J_{sc}, and FF values are listed in Supporting Information Table S2. [Color figure can be viewed in the online issue, which is available at wileyonlinelibrary.com.]

PCE, whereas the addition of 5% *rra*-P3HT does not significantly affect the PCE value. With more *rra*-P3HT added, the performance is severely declined.

The long-term stability of the solar cells was further examined. The devices were stored in the dark in a glove-box to prevent light and oxygen, and the dependence of PCE values on time was measured. The PCEs of the most efficient devices are shown in Figure 6. Although the PCE of B-100 is slightly higher than that of B-95 initially, it turns to be lower than that of B-95 after 5 days and decays to 2.04% within 50 days (62.9% of the initial value). The PCE of B-95 also decays but with a slower rate, down to 2.78% after 50 days (85.2% of the initial value). This demonstrates that the stability of solar cell is improved by introduction of amorphous polymer into the active layer. For B-80 and B-90, the PCE increases to a maximum after 5 days and then slightly decreased with time. It is possible that 10 min at 140 °C is too short to appropriately anneal B-80 and B-90 films due to the large amount of *rra*-P3HT that retard the necessary structural re-arrangement of *rr*-P3HT and PCBM from as-cast state, and it takes extra more days at room temperature to reach the optimum morphology.[33] Though the efficiency is low, the performance of the solar cells is rather stable for such a high fraction of amorphous polymer. The detailed time-dependent maximum PCE and average PCE values from at least five devices on two different substrates for each sample are provided in Supporting Information Table S3. Supporting Information Figure S2 shows the average PCEs as functions of time and the trends are consistent with the most efficient ones.

Exciton dissociation in organic photovoltaics has conventionally been considered to occur at the interface between pure donor and acceptor domains.[6,44] Recently, it has been shown that the donor/acceptor intermixed phase can facilitate exciton quenching and charge extraction, which is one of the key factors that affects short circuit current (J_{sc}) and fill factor (FF) of bulk heterojunction solar cells.[6,8,45] In other words, in addition to the well-packed P3HT and clustered PCBM domains that act as hole and electron transporting pathways respectively, an intermixed P3HT/PCBM phase is required for free charges to be efficiently generated. Because crystallization or close packing generally exclude impurities and thus lead to pure phases, amorphous P3HT is more capable of incorporating fullerene molecules to form intermixed phases. The addition of *rra*-P3HT, on one hand, reduces the fraction of pure P3HT crystalline phase, which is unfavorable for hole transport. On the other hand, it can more effectively maintain the fraction of the P3HT/PCBM intermixed phase for charge generation. This may be why B-95 exhibits an initial PCE similar to that of B-100.

The formation of intermixed P3HT/PCBM phase can further explain why B-95 is more stable than B-100. The parameters of the fill factor (FF), open circuit voltage (V_{oc}), and short circuit current (J_{sc}) of B-95 and B-100 are listed in Table S2. V_{oc} is essentially the same for both samples and nearly independent of time. The initial FF and J_{sc} values of B-95 and B-100 are comparable but the values decay more rapidly with time for B-100. The FF of B-100 decreases to 70.4% of the initial value after 50 days while that of B-95 is nearly unchanged. The J_{sc} decreases to 78.5 and 84.4% of the initial values for B-100 and B-95 after 50 days, respectively. We attribute the improvement in the stability of B-95 to the capability of amorphous *rra*-P3HT to thermodynamically mix with PCBM,[39] which retards the crystallization-induced phase separation and thus prevents the efficiency of charge separation from a rapid decay with increasing time. This point will be confirmed by the following time-dependent structural characterization.

Time-Dependent Structure in Thin Films

The GISAXS profiles of pure *rra*-P3HT (P-0) and *rr*-P3HT (P-100) thin films extracted from q_y scans at $q_z = 0.026$ Å^{-1} after thermal annealing at 140 °C for 10 min are shown in

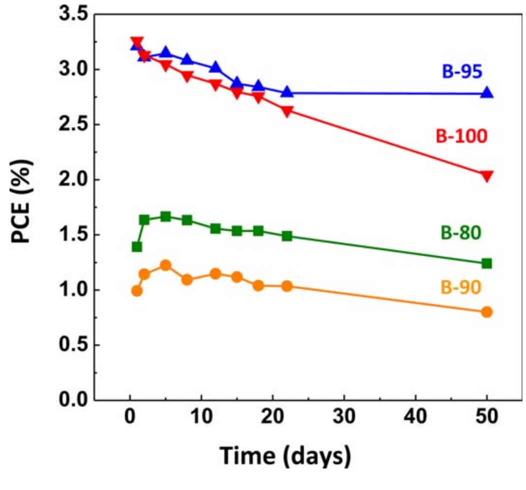

FIGURE 6 Time-dependent power conversion efficiency (PCE) of B-80, B-90, B-95, and B-100 devices. The data are from the most efficient devices. [Color figure can be viewed in the online issue, which is available at wileyonlinelibrary.com.]

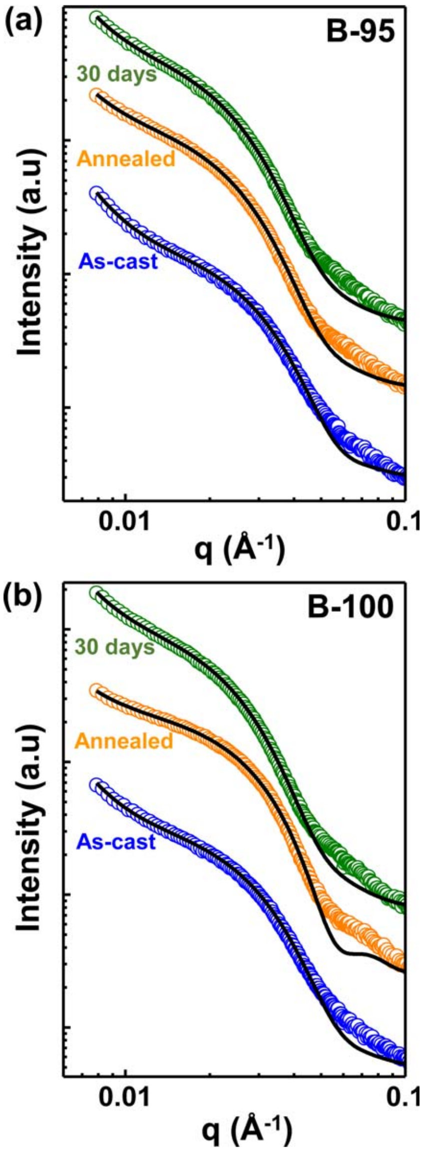

FIGURE 7 GISAXS profiles of (a) B-95 and (b) B-100 samples before thermal annealing, after annealing at 140 °C for 10 min, and 30 days after annealing. Model fits are shown as the solid lines. [Color figure can be viewed in the online issue, which is available at wileyonlinelibrary.com.]

Supporting Information Figure S3(a,b). The intensities of both curves monotonically decrease with increasing wave vector q and no significant structural information can be observed from the data. This is rational for P-0 because the entire sample is amorphous. For P-100 whose crystalline domains are supposed to be distinguished from amorphous phase in this q range,[25] the featureless profile is possibly because the electron density contrast between crystalline and amorphous phases are still too low to generate detectable characteristic scattering from crystallites. The GISAXS data of B-0 film where PCBM is blended with *rra*-P3HT is shown in Supporting Information Figure S3(c). Although PCBM diffraction ring appears in the GIWAXS pattern [Fig. 3(e)], which indicates some regular packing in PCBM clusters, there is no scattering feature in the GISAXS profile either. It has been shown that PCBM and amorphous P3HT are miscible and PCBM should dissolve in amorphous P3HT.[24,43] The featureless profile may be due to the lack of scattering contrast between PCBM/*rra*-P3HT intermixed phase and PCBM clusters.

GISAXS profiles of B-95 and B-100 obtained before thermal annealing, after annealing at 140 °C for 10 min, and 30 days after the annealing are shown in Figure 7. Different from P-0, P-100, and B-0 thin films, clear shoulders can be seen between $q = 0.02\text{–}0.04$ Å^{-1}. Such a scattering profile has previously been interpreted to originate either from PCBM clusters[20,46–49] or from the spatial arrangement of P3HT crystallites.[25,50] Since the scattering shoulder is absent in B-0 sample that contains PCBM clusters [Supporting Information Fig. S3(c)], we suggest that the shoulders are caused by P3HT crystallites, which appear in the profiles of B-95 and B-100 samples due to the increasing contrast between pure P3HT crystallites and PCBM/amorphous P3HT intermixed phases, in comparison to P-100 sample that contains P3HT crystallites but without the shoulder [Supporting Information Fig. S3(b)].[24] Furthermore, the shoulder slightly shifts to lower q after thermal annealing, corresponding an increase in size. The shoulder can thus be rationally ascribed to the scattering form factor of P3HT crystallites which grow after thermal annealing.

In addition to the shoulders, it is worth noting that the slopes of the curves at q below 0.02 Å^{-1} are dependent on sample treatments. In both B-95 and B-100, the slope is apparently larger before annealing, and it decreases after annealing and then increases again 30 days after annealing. The low-q scattering is generally contributed from large scatterers and in the present cases, the change of intensity in low q range should be caused by the varying scales of phase separation in P3HT/PCBM blends under different treatments, specifically, the phase primarily composed of P3HT crystallites in contrast to the phase combining pure PCBM clusters and PCBM/amorphous P3HT intermixed domains. Larger phase separation scales generally lead to a higher slope of scattering curves at low q.

To quantify P3HT crystallite sizes and the phase separation scales, we model the GISAXS profiles with appropriate functions. For the approximate estimation and comparison of P3HT crystallite sizes from intermediate to high q, we assume the crystallites are polydisperse spherical particles. The scattering function is denoted as I^S and given by[51]

$$I^S(q)=(\Delta\rho)^2\left(\frac{4}{3}\pi\right)^2\int_0^\infty f(R)R^6F^2(qR)\mathrm{d}R \qquad (1)$$

Here $\Delta\rho$ is the scattering contrast and R is the radius of the particle. The scattering amplitude for a particle $F(qR)$ is given by

$$F(qR)=\frac{3[\sin(qR)-qR\cos(qR)]}{(qR)^3} \qquad (2)$$

TABLE 1 Fitting Parameters from GISAXS and SAXS Modeling for B-95 and B-100 Samples

Sample	Treatment	R_0 (nm)	ξ (nm)	p
Thin films (GISAXS)				
B-95	As-cast	6.3	94.8	0.23
	Annealed	7.0	48.3	0.26
	30 days	7.0	73.7	0.28
B-100	As-cast	6.2	82.4	0.23
	Annealed	7.2	41.2	0.15
	30 days	7.2	88.8	0.26
Bulk samples annealed at 140 °C (SAXS)				
B-95	0 min	7.6	19.1	0.31
	10 min	8.0	17.0	0.26
	45 min	8.1	16.9	0.25
	120 min	8.4	30.8	0.21
B-100	0 min	5.9	31.5	0.41
	10 min	6.6	30.4	0.37
	45 min	6.8	29.5	0.35
	120 min	6.7	40.0	0.31

The polydispersity in radius $f(R)$ is accounted for by a Schulz distribution equation:[52]

$$f(R)=\left(\frac{z+1}{R_0}\right)^{z+1}\frac{R^z}{\Gamma(z+1)}\exp\left(-(z+1)\frac{R}{R_0}\right) \tag{3}$$

In the above expression, R_0 is the average radius and Γ is gamma function. The polydispersity p is given by

$$p=\frac{1}{\sqrt{z+1}} \tag{4}$$

To estimate the phase separation scale revealed at low q, we chose Debye–Anderson–Brumberger (DAB) model which is commonly used for randomly distributed two-phase systems,[53]

$$I^{\mathrm{DAB}}(q)=\frac{A\xi^3}{\left[1+(q\xi)^2\right]^2} \tag{5}$$

The factor A is treated as an independent fitting parameter here. ξ is the correlation length which is inversely proportional to the total interfacial area between phases. A larger ξ, that is, smaller total interfacial area, indicates a greater phase separation scale. We combine eq. 1 and 5, that is, $I(q)=I^{S}(q)+I^{\mathrm{DAB}}(q)$, to model the GISAXS profiles, which was conducted using the analysis package provided by NIST with IGOR Pro software.[54] The fits are shown in Figure 7 as solid lines through the data and the fitting parameters are listed in Table 1.

In both annealed B-95 and B-100 films, the average radius of P3HT crystallites (~7 nm) is larger than that of as-cast films (~6 nm), and does not significantly change after 30 days. It has been well known that thermal annealing can result in a thickening of polymer crystallites toward thermodynamically more stable crystal structure. The growth of the crystallites is consistent with the GIWAXS data shown in Supporting Information Figure S1 where the sharper diffraction peaks of P3HT crystallites after thermal annealing imply a larger size of crystallites. Note that the average radius of the crystallites is within the exciton diffusion length of P3HT (5–10 nm),[2] which is favorable for the excitons to reach P3HT/PCBM interfaces for dissociation before recombination. Also note that it has been observed that P3HT generally forms crystalline nanofibers with ~20 nm width. It is possible that the P3HT nanofibers are formed by the 1D arrangement of the small crystallites.[25,50]

In contrast to the dimension change of crystallites, the scale of phase separation domains ξ for as-cast films is large, 94.8 and 82.4 nm for B-95 and B-100, respectively. After thermal annealing, ξ greatly reduces to ~ 40–50 nm and then increases again to 73.7 and 88.8 nm for B-95 and B-100, respectively, after 30 days. We suggest that in as-cast films, solvent evaporation causes the formation of small P3HT crystallites that mix with amorphous P3HT and the incorporated PCBM to form large domains segregated from PCBM-rich domains. Such a phase separation domain should be in a kinetically frozen state with solvent effects involved, including the interactions of the solvent with P3HT and PCBM, and the solvent evaporation rate. Short thermal annealing results in a thickening of P3HT crystallites as well as an enhancement of crystallinity, and thus a dense P3HT crystalline domain is developed. Since small molecules are able to move through the free volume of amorphous P3HT even at room temperature, with increasing time, PCBM tends to move out from the kinetically frozen intermixed amorphous regions between P3HT crystallites where PCBM concentration is originally above the threshold, which in turn causes the aggregation of PCBM and the formation of relatively large P3HT crystallite-rich domains. The above structural evolution is illustrated in Figure 8. Note that in B-100, ξ increases slightly more than that of B-95 after 30 days. The change of ξ is closely related to the PCE of the corresponding devices. For as-cast films, because of the low crystallinity of P3HT and the loosely packed small P3HT crystallites, the charge carrier mobility is low, which explains the inferior efficiency for as-cast films.[55] After thermal annealing, P3HT crystallites form well defined channels with appropriate dimension that facilitates charge generation and transport, thus causing the maximum efficiency. As time increases, the aggregation of PCBM reduces the interfacial area between P3HT and PCBM, which is unfavorable for exciton dissociation and, therefore, the efficiency decays with time.

Time-Dependent Structure at High Temperature

In the preceding sections, the samples were shortly thermal-annealed and then kept at room temperature for studying the structural evolution in thin films. At room temperature, the relaxation of molecules is slow so that the structure only slightly changes even over 30 days. To accelerate the process, B-95 and B-100 bulk samples were maintained at 140 °C where the molecular motion is much faster and we should

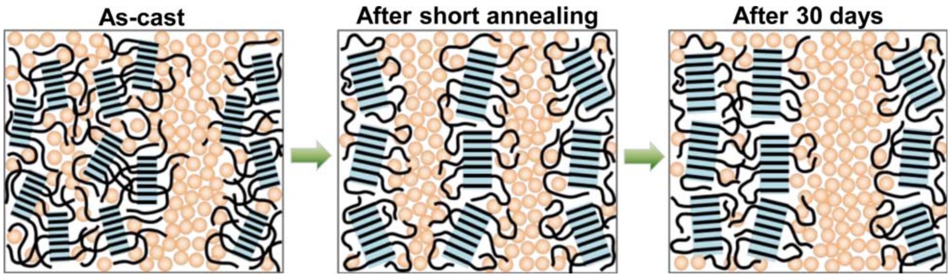

FIGURE 8 Schematics for the morphology in as-cast film, after annealing, and long time after annealing. For as-cast film, small P3HT crystallites loosely cluster with PCBM. After annealing, P3HT crystallites grow and form fine continuous channels. As time increases, PCBM tends to aggregate, which gives rise to large phase separation domains. [Color figure can be viewed in the online issue, which is available at wileyonlinelibrary.com.]

see the same morphological transition in a shorter time. The reason for the use of bulk samples is that transmission mode SAXS instead of GISAXS can be adopted to probe the structures, which increases the number of atoms X-ray can interact with as well as prevents the possible interference of the reflection signal from the substrate in GISAXS measurements. Figure 9 shows the SAXS data of B-95 and B-100 bulk samples annealed at 140 °C for 0, 10, 45, and 120 min and the fits based on the same combination of eqs 1 and 5 are shown as the solid curves. The fitting parameters are listed in Table 1. Similarly, the average radius of P3HT crystallites increases after heating. After heating for 10 min, the correlation length ξ also turns to be smaller than that of as-cast bulk samples but the decrease is very limited compared to that of thin films. It is possible that solvent evaporation rate is slower during the preparation of bulk samples and thus a phase separation structure more toward thermodynamic equilibrium has been achieved in the as-cast bulk samples. Between 10 and 45 min, ξ is nearly unchanged for both B-95 and B-100. After 120 min, ξ greatly increases, from 17 to 30.8 nm for B-95 and from 30 to 40 nm for B-100, respectively, confirming that highly crystalline P3HT aggravates the phase separation due to the exclusion of PCBM from closely packed P3HT crystals, which, however, can be alleviated by the addition of amorphous P3HT that has more room to accommodate PCBM.

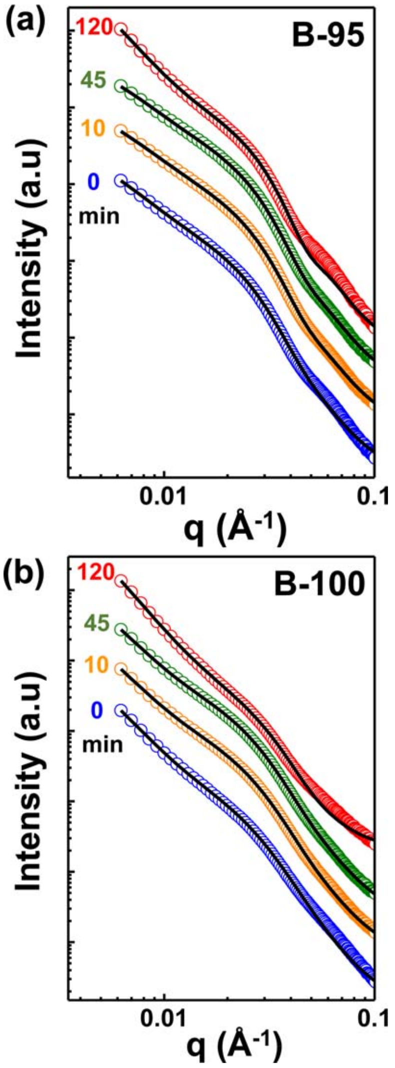

FIGURE 9 SAXS profiles of (a) B-95 and (b) B-100 bulk samples annealed at 140 °C for 0, 10, 45, and 120 min. Model fits are shown as the solid lines. [Color figure can be viewed in the online issue, which is available at wileyonlinelibrary.com.]

In addition to the nanoscale domains analyzed by SAXS, we have also used optical microscopy to inspect macroscale phase separation at high temperature. Figure 10 displays the optical images of B-95 and B-100 samples annealed at 140 °C for 0, 45, and 120 min. As shown in Figure 10(a,d), there are no large aggregates at the initial stage of both samples. After 45 min [Fig. 10(b,e)], some dark dots appear in the images of B-100 and only few of such dots are found in B-95. Further increasing time to 120 min, slightly more aggregates are seen in B-95 [Fig. 10(c)] but a great number of needle-like aggregates with a size larger than 100 μm grow in B-100 [Fig. 10(f)]. The large aggregates are PCBM crystals,[25,56] which is supported by the WAXS data shown in Supporting Information Figure S4 where the sharp PCBM characteristic peaks are observed after 120-min annealing. The aggregation of PCBM leads to a greater phase separation scale, thus causing the upturns in low q range as shown in Figure 9. The above observation confirms that amorphous P3HT can retard the aggregation of PCBM, which is

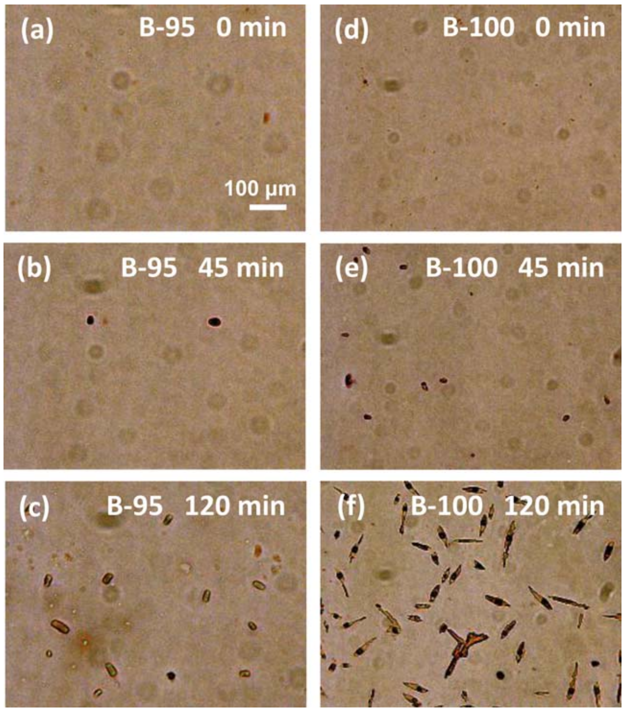

FIGURE 10 Optical microscopy images of (a–c) B-95 and (d–f) B-100 samples annealed at 140 °C for 0, 45, and 120 min. [Color figure can be viewed in the online issue, which is available at wileyonlinelibrary.com.]

consistent with the AFM and the scattering results as well as the trend of the performance of B-95- and B-100-based solar cells.

CONCLUSIONS

For bulk heterojunction polymer/fullerene solar cells, high polymer crystallinity is crucial for performing a high PCE, because it can facilitate the charge carrier transport through the route of π-π stacking. In this work, we have clearly shown that amorphous regions that can intermix with fullerene is also important, which not only promotes the charge carrier separation process but provides a stable structure that prevents the rapid decay of performance. We demonstrated that by the addition of a small amount amorphous P3HT into semicrystalline P3HT, the initial PCE is nearly the same as that of pure semi-crystalline P3HT. The long-term stability, however, is improved. Crystalline P3HT rejects PCBM upon crystallization and may inevitably force PCBM to aggregate, whereas amorphous P3HT can mix with PCBM so that a more stable morphology can form to retard large-scaled phase separation that is generally regarded as one of the major causes for solar cell deterioration. The findings suggest that thermodynamically miscible donor/acceptor systems that are able to form stable structure optimal for charge carrier separation and transportation will be the key en route to highly stable organic solar cells.

ACKNOWLEDGMENTS

This work was financially supported by the grant from the Ministry of Education, Taiwan. The authors acknowledge NSRRC, Taiwan, for facilitating the GISAXS and SAXS experiments. The assistance in scattering experiments from U-Ser Jeng of NSRRC is also acknowledged.

REFERENCES AND NOTES

1 G. Yu, J. Gao, J. C. Hummelen, F. Wudl, A. J. Heeger, *Science* **1995**, *270*, 1789–1791.

2 P. E. Shaw, A. Ruseckas, I. D. W. Samuel, *Adv. Mater.* **2008**, *20*, 3516–3520.

3 F. Liu, Y. Gu, J. W. Jung, W. H. Jo, T. P. Russell, *J. Polym. Sci. Part B: Polym. Phys.* **2012**, *50*, 1018–1044.

4 F. Padinger, R. S. Rittberger, N. S. Sariciftci, *Adv. Funct. Mater.* **2003**, *13*, 85–88.

5 Y. Kim, S. A. Choulis, J. Nelson, D. D. C. Bradley, S. Cook, J. R. Durrant, *J. Mater. Sci.* **2005**, *40*, 1371–1376.

6 P. Westacott, J. R. Tumbleston, S. Shoaee, S. Fearn, J. H. Bannock, J. B. Gilchrist, S. Heutz, J. deMello, M. Heeney, H. Ade, J. Durrant, D. S. McPhail, N. Stingelin, *Energy Environ. Sci.* **2013**, *6*, 2756–2764.

7 M. Scarongella, A. A. Paraecattil, E. Buchaca-Domingo, J. D. Douglas, S. Beaupre, T. McCarthy-Ward, M. Heeney, J. E. Moser, M. Leclerc, J. M. J. Frechet, N. Stingelin, N. Banerji, *J. Mater. Chem. A* **2014**, *2*, 6218–6230.

8 C. Kastner, S. Rathgeber, D. A. M. Egbe, H. Hoppe, *J. Mater. Chem. A* **2013**, *1*, 3961–3969.

9 W. Ma, J. Y. Kim, K. Lee, A. J. Heeger, *Macromol. Rapid Commun.* **2007**, *28*, 1776–1780.

10 T. Xiao, H. Xu, G. Grancini, J. Mai, A. Petrozza, U. S. Jeng, Y. Wang, X. Xin, Y. Lu, N. S. Choon, H. Xiao, B. S. Ong, X. Lu, N. Zhao, *Sci. Rep.* **2014**, *4*, 5211.

11 Z. Zhang, F. Lin, H. C. Chen, H. C. Wu, C. L. Chung, C. Lu, S. H. Liu, S. H. Tung, W. C. Chen, K. T. Wong, P. T. Chou, *Energy Environ. Sci.* **2015**, *8*, 552–557.

12 Y. Liu, J. Zhao, Z. Li, C. Mu, W. Ma, H. Hu, K. Jiang, H. Lin, H. Ade, H. Yan, *Nat. Commun.* **2014**, *5*, 5293.

13 S. H. Liao, H. J. Jhuo, P. N. Yeh, Y. S. Cheng, Y. L. Li, Y. H. Lee, S. Sharma, S. A. Chen, *Sci. Rep.* **2014**, *4*, 6813.

14 B. Kan, M. Li, Q. Zhang, F. Liu, X. Wan, Y. Wang, W. Ni, G. Long, X. Yang, H. Feng, Y. Zuo, M. Zhang, F. Huang, Y. Cao, T. P. Russell, Y. Chen, *J. Am. Chem. Soc.* **2015**, *137*, 3886–3893.

15 W. Yu, L. Huang, D. Yang, P. Fu, L. Zhou, J. Zhang, C. Li, *J. Mater. Chem. A* **2015**, *3*, 10660–10665.

16 M. Jørgensen, K. Norrman, S. A. Gevorgyan, T. Tromholt, B. Andreasen, F. C. Krebs, *Adv. Mater.* **2012**, *24*, 580–612.

17 J. Jo, S. S. Kim, S. I. Na, B. K. Yu, D. Y. Kim, *Adv. Funct. Mater.* **2009**, *19*, 866–874.

18 M. Shin, H. Kim, J. Park, S. Nam, K. Heo, M. Ree, C. S. Ha, Y. Kim, *Adv. Funct. Mater.* **2010**, *20*, 748–754.

19 S. Bertho, G. Janssen, T. J. Cleij, B. Conings, W. Moons, A. Gadisa, J. D'Haen, E. Goovaerts, L. Lutsen, J. Manca, D. Vanderzande, *Sol. Energy Mater. Sol. Cells* **2008**, *92*, 753–760.

20 C. Y. Chen, C. S. Tsao, Y. C. Huang, H. W. Liu, W. Y. Chiu, C. M. Chuang, U. S. Jeng, C. J. Su, W. R. Wu, W. F. Su, L. Wang, *Nanoscale* **2013**, *5*, 7629–7638.

21 H. D. Keith, F. J. Padden, *J. Appl. Phys.* **1964**, *35*, 1270–1285.

22 A. C. Mayer, M. F. Toney, S. R. Scully, J. Rivnay, C. J. Brabec, M. Scharber, M. Koppe, M. Heeney, I. McCulloch, M. D. McGehee, *Adv. Funct. Mater.* **2009**, *19*, 1173–1179.

23 N. C. Miller, S. Sweetnam, E. T. Hoke, R. Gysel, C. E. Miller, J. A. Bartelt, X. Xie, M. F. Toney, M. D. McGehee, *Nano Lett.* **2012**, *12*, 1566–1570.

24 H. W. Ro, B. Akgun, B. T. O'Connor, M. Hammond, R. J. Kline, C. R. Snyder, S. K. Satija, A. L. Ayzner, M. F. Toney, C. L. Soles, D. M. DeLongchamp, *Macromolecules* **2012**, *45*, 6587–6599.

25 P. Kohn, Z. Rong, K. H. Scherer, A. Sepe, M. Sommer, P. Müller-Buschbaum, R. H. Friend, U. Steiner, S. Hüttner, *Macromolecules* **2013**, *46*, 4002–4013.

26 B. J. Kim, Y. Miyamoto, B. Ma, J. M. J. Fréchet, *Adv. Funct. Mater.* **2009**, *19*, 2273–2281.

27 G. Griffini, J. D. Douglas, C. Piliego, T. W. Holcombe, S. Turri, J. M. J. Fréchet, J. L. Mynar, *Adv. Mater.* **2011**, *23*, 1660–1664.

28 B. H. Johnson, E. Allagoa, R. L. Thomas, G. Stettler, M. Wallis, J. H. Peel, T. Adalsteinsson, B. J. McNelis, R. P. Barber. Jr, *Sol. Energy Mater. Sol. Cells* **2010**, *94*, 537–541.

29 Y. J. Cheng, C. H. Hsieh, P. J. Li, C. S. Hsu, *Adv. Funct. Mater.* **2011**, *21*, 1723–1732.

30 Z. Li, H. C. Wong, Z. Huang, H. Zhong, C. H. Tan, W. C. Tsoi, J. S. Kim, J. R. Durrant, J. T. Cabral, *Nat. Commun.* **2013**, *4*, 2227.

31 N. Sary, F. Richard, C. Brochon, N. Leclerc, P. Lévêque, J. N. Audinot, S. Berson, T. Heiser, G. Hadziioannou, R. Mezzenga, *Adv. Mater.* **2010**, *22*, 763–768.

32 J. H. Tsai, Y. C. Lai, T. Higashihara, C. J. Lin, M. Ueda, W. C. Chen, *Macromolecules* **2010**, *43*, 6085–6091.

33 C. H. Woo, B. C. Thompson, B. J. Kim, M. F. Toney, J. M. J. Fréchet, *J. Am. Chem. Soc.* **2008**, *130*, 16324–16329.

34 S. Ebadian, B. Gholamkhass, S. Shambayati, S. Holdcroft, P. Servati, *Sol. Energy Mater. Sol. Cells* **2010**, *94*, 2258–2264.

35 M. Campoy-Quiles, Y. Kanai, A. El-Basaty, H. Sakai, H. Murata, *Org. Electron.* **2009**, *10*, 1120–1132.

36 U. S. Jeng, C. H. Su, C. J. Su, K. F. Liao, W. T. Chuang, Y. H. Lai, J. W. Chang, Y. J. Chen, Y. S. Huang, M. T. Lee, K. L. Yu, J. M. Lin, D. G. Liu, C. F. Chang, C. Y. Liu, C. H. Chang, K. S. Liang, *J. Appl. Crystallogr.* **2010**, *43*, 110–121.

37 T. Adachi, J. Brazard, R. J. Ono, B. Hanson, M. C. Traub, Z. Q. Wu, Z. Li, J. C. Bolinger, V. Ganesan, C. W. Bielawski, D. A. Vanden Bout, P. F. Barbara, *J. Phys. Chem. Lett.* **2011**, *2*, 1400–1404.

38 J. Clark, J. F. Chang, F. C. Spano, R. H. Friend, C. Silva, *Appl. Phys. Lett.* **2009**, *94*, 163306.

39 P. J. Brown, D. S. Thomas, A. Köhler, J. S. Wilson, J. S. Kim, C. M. Ramsdale, H. Sirringhaus, R. H. Friend, *Phys. Rev. B* **2003**, *67*, 064203.

40 Y. Zhang, H. L. Yip, O. Acton, S. K. Hau, F. Huang, A. K. Y. Jen, *Chem. Mater.* **2009**, *21*, 2598–2600.

41 B. Watts, W. J. Belcher, L. Thomsen, H. Ade, P. C. Dastoor, *Macromolecules* **2009**, *42*, 8392–8397.

42 F. C. Jamieson, E. B. Domingo, T. McCarthy-Ward, M. Heeney, N. Stingelin, J. R. Durrant, *Chem. Sci.* **2012**, *3*, 485–492.

43 D. Chen, A. Nakahara, D. Wei, D. Nordlund, T. P. Russell, *Nano Lett.* **2011**, *11*, 561–567.

44 M. C. Scharber, N. S. Sariciftci, *Prog. Polym. Sci.* **2013**, *38*, 1929–1940.

45 J. A. Bartelt, Z. M. Beiley, E. T. Hoke, W. R. Mateker, J. D. Douglas, B. A. Collins, J. R. Tumbleston, K. R. Graham, A. Amassian, H. Ade, J. M. J. Fréchet, M. F. Toney, M. D. McGehee, *Adv. Energy Mater.* **2013**, *3*, 364–374.

46 J. W. Kiel, A. P. R. Eberle, M. E. Mackay, *Phys. Rev. Lett.* **2010**, *105*, 168701.

47 H. C. Liao, C. S. Tsao, T. H. Lin, C. M. Chuang, C. Y. Chen, U. S. Jeng, C. H. Su, Y. F. Chen, W. F. Su, *J. Am. Chem. Soc.* **2011**, *133*, 13064–13073.

48 W. R. Wu, U. S. Jeng, C. J. Su, K. H. Wei, M. S. Su, M. Y. Chiu, C. Y. Chen, W. B. Su, C. H. Su, A. C. Su, *ACS Nano* **2011**, *5*, 6233–6243.

49 H. C. Liao, C. S. Tsao, Y. T. Shao, S. Y. Chang, Y. C. Huang, C. M. Chuang, T. H. Lin, C. Y. Chen, C. J. Su, U. S. Jeng, Y. F. Chen, W. F. Su, *Energy Environ. Sci.* **2013**, *6*, 1938–1948.

50 Y. Gu, C. Wang, F. Liu, J. Chen, O. E. Dyck, G. Duscher, T. P. Russell, *Energy Environ. Sci.* **2014**, *7*, 3782–3790.

51 M. Kotlarchyk, S. H. Chen, *J. Chem. Phys.* **1983**, *79*, 2461–2469.

52 G. V. Schulz, *Z. Phys. Chem. B Chem. E* **1939**, *43*, 25–46.

53 P. Debye, H. R. Anderson, H. Brumberger, *J. Appl. Phys.* **1957**, *28*, 679–683.

54 S. R. Kline, *J. Appl. Crystallogr.* **2006**, *39*, 895–900.

55 F. Laquai, D. Andrienko, R. Mauer, P. W. M. Blom, *Macromol. Rapid Commun.* **2015**, *36*, 1001–1025.

56 A. Swinnen, I. Haeldermans, M. vande Ven, J. D'Haen, G. Vanhoyland, S. Aresu, M. D'Olieslaeger, J. Manca, *Adv. Funct. Mater.* **2006**, *16*, 760–765.